

CZECH TECHNICAL UNIVERSITY IN PRAGUE  
FACULTY OF NUCLEAR SCIENCE AND  
PHYSICAL ENGINEERING

Department of Physics



Polarization of  $J/\psi$  in STAR  
experiment

RESEARCH THESIS

Author: Kamila Vysoká  
Supervisor: Mgr. Jaroslav Bielčík, Ph.D.  
Konsultant: Dr. Barbara Trzeciak  
Academic year: 2013/2014

## Prehlásenie

Prehlasujem, že som svoju bakalársku prácu vypracovala samostatne a použila som len literatúru a publikácie uvedené v priloženom zozname.

Nemám závažný dôvod proti použitiu tohoto školského diela v zmysle §60 Zákona č.121/1200Sb., o autorskom práve, o právach súvisiacich s autorským právom a o zmene niektorých zákonov (autorský zákon).

V Prahe dňa .....



*Názov práce:* **Polarizácia  $J/\psi$  v experimente STAR**

*Autor:* Kamila Vysoká

*Obor:* Experimentální jaderná a částicová fyzika

*Druh práce:* Výzkumný úkol

*Vedoucí práce:* Mgr. Jaroslav Bielčík, Ph.D.

Katedra fyziky, Fakulta jaderná a fyzikálně inženýrská,  
České vysoké učení technické v Praze.

### **Abstrakt:**

Rôzne modely môžu popísať produkciu mezónou  $J/\psi$ . Meranie účinného prierezu nebolo dostatočne presné, aby bolo možné určiť, ktorý z daných modelov popisuje reálnu produkciu lepšie. Následne sa pristúpilo k možnosti, že meranie polarizácie  $J/\psi$  bude schopné rozlíšiť medzi modelmi. Za týmto účelom je potrebné, aby bolo dosiahnuté presné meranie  $J/\psi$  s vysokou priečnou hybnosťou. Meranie polarizačného parametru  $\lambda_\theta$  na experimentoch STAR a PHENIX môže naznačovať trend smerom k pozdĺžnej polarizácii pri zvyšujúcej sa priečnej hybnosti. Tento argument je ale platný iba v prípade, že azimutálny uhol  $\varphi$  má plochú distribúciu.

*Kľúčová slova:* urýchľovač RHIC, detektor STAR, kvarkónia, polarizácia,  $J/\psi$

*Title:* **Polarization of  $J/\psi$  in STAR experiment**

*Author:* Kamila Vysoká

### **Abstract:**

Various models can describe the production of  $J/\psi$  meson. Measuring the cross section was not precise enough to determine which of the given models describes the real production better. Later the possibility that measuring the polarization  $J/\psi$  will be able to distinguish between models has come to prominence. For this purpose it is necessary to achieve the accurate measurement of  $J/\psi$  with high transverse momentum. Polarization measurements of  $\lambda_\theta$  parameter in STAR and PHENIX experiments may indicate a trend towards the longitudinal polarization for an increasing transverse momentum. Nevertheless, this argument is valid only if the azimuthal angle  $\varphi$  has flat distribution.

*Keywords:* accelerator RHIC, STAR detector, quarkonium, polarization,  $J/\psi$



## **Ancknowledgement**

I would like to thank my supervisor Jaroslav Bielčík, my consultant Barbara Trzeciak and my husband Jan Vysoký for their support, expert advice and patience.



# Contents

<b>1</b>	<b>Introduction</b>	<b>12</b>
1.1	History . . . . .	12
1.2	Time evolution . . . . .	12
1.3	Nuclear modification factor . . . . .	13
1.4	Phase diagram of nuclear mater . . . . .	14
<b>2</b>	<b>The STAR experiment at accelerator RHIC</b>	<b>16</b>
2.1	Relativistic Heavy Ion Collider, RHIC . . . . .	16
2.2	STAR detector . . . . .	20
2.2.1	Overview of subsystems of the STAR experiment . . . . .	21
<b>3</b>	<b>Production mechanism of <math>J/\psi</math></b>	<b>26</b>
3.1	Introduction . . . . .	26
3.1.1	Reference frame . . . . .	28
3.2	Tevatron and LHC measurement of polarization . . . . .	29
3.3	STAR measurement of polarization . . . . .	29
<b>4</b>	<b>Analysis of simulated data</b>	<b>32</b>
4.1	Methods of analysis of polarization . . . . .	32
4.2	Embedding . . . . .	32
4.3	$\varphi$ measurement . . . . .	34





# List of Figures

1.1	Space time evolution of collision . . . . .	13
1.2	The phase diagram of nuclear matter . . . . .	14
2.1	Schema of RHIC accelerator . . . . .	17
2.2	Scheme of STAR experiment . . . . .	20
2.3	Scheme of TPC . . . . .	22
2.4	A collision of gold nuclei recorded in TPC . . . . .	24
3.1	$p_T$ spectrum of $J/\psi$ . . . . .	27
3.2	Production models . . . . .	27
3.3	Reference frame . . . . .	28
3.4	Polarization angles . . . . .	29
3.5	Polarization measurements at LHC and TEVATRON . . . . .	30
3.6	Polarization measurements at STAR . . . . .	31
4.1	Embedding flowchart . . . . .	33
4.2	Distribution of angle $\varphi$ in simulate data with no additional cuts . . . . .	34
4.3	F . . . . .	36
4.4	F . . . . .	36



# List of Tables

2.1	Parameters of RHIC accelerator . . . . .	18
2.2	List of runs on RHIC accelerator . . . . .	19
4.1	Track quality and acceptance cuts . . . . .	35



# Chapter 1

## Introduction

### 1.1 History

In year 1964 Sheldon Lee Glashow and James Bjorken suggested an additional fourth quark, which they named charm because they were charmed with a symmetry that it brings to the world of subnuclear physics.

A name of meson  $J/\psi$  has two letters because its discovery was announced simultaneously on Sunday November 10, 1974 by two different physics groups.

The group from research facility SLAC under the leadership of Burton Richter found it while searching for the charm quark around the energy of 3 GeV. Richter wanted to name the new particle " $SP$ ", after the accelerator SPEAR at which was the particle discovered, but the name was not received with much enthusiasm. Therefore, the name was changed to a Greek letter  $\psi$ . By coincidence in English transcription of this Greek letter  $PSI$  the first two letters read in reverse order give the original name " $SP$ ".

MIT group under the leadership of Samuel Chao Chung Ting working on experiment in Brookhaven announced new particle with peak at 3.105 GeV. Ting assigned it a name " $J$ ", probably because it is a letter in the alphabet one before " $K$ " already used for a known strange meson. Maybe by another coincidence maybe not the letter " $J$ " strongly resembles a Chinese ideogram for Tings name ( $\mathcal{T}$ ) and also it is a first letter of a name of his oldest daughters Jeanne. [1]

### 1.2 Time evolution

Let us have a collision of two nuclei, which move at about the speed of light. In Figure 1.1 this particle collision is shown. The collision occurs at time  $t = 0$ , at which also the position coordinates have zero values. The upper half corresponds

to the time after the collision and the bottom half corresponds to the time before it. The upper half outlines the forming of a drop of hot and dense matter, which develops and expands over time to the point where, after various processes, occurs a particle freeze-out. For all relativistic particles there applies an equation

$$\sqrt{t^2 c^2 - z^2} = \tau, \quad (1.1)$$

where  $\tau$  is a proper time for the particle. If for any particle its own time equals zero, the particle is moving at the speed of light and its trajectory lies on the light cone.

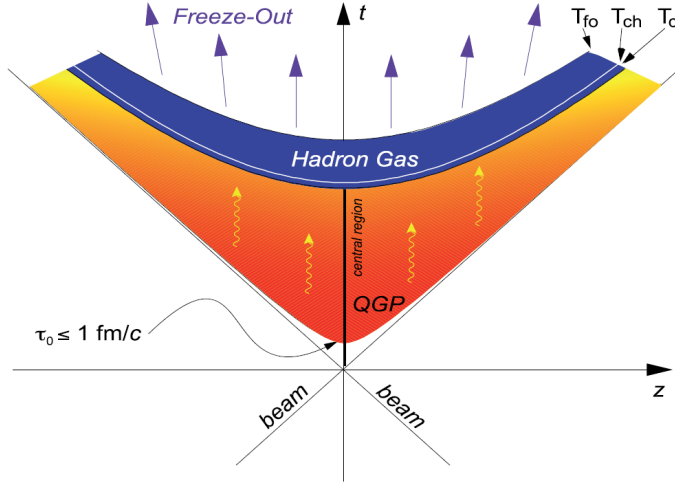


Figure 1.1: Time evolution of a collision is displayed inside the light cone, including a formation time of a quark-gluon plasma, a critical temperature and a particle freeze-out [2]

We can define new variables  $x_{\pm}$  in the context of their relationship to the beams of the light cone. They are defined as

$$x_+ = tc + z \quad x_- = tc - z. \quad (1.2)$$

These coordinates are suitable for the description of ultra-relativistic particles, because when relations (1.2) are multiplied together we get the expression for the square of the relativistic particle own time.

### 1.3 Nuclear modification factor

An observable comparing different conditions in collisions of protons and atomic nuclei is called a nuclear modification factor, and for the given hadron  $h$  it is defined by the equation

$$R_{AA}^h(y, p_T; W) = \frac{\frac{d\sigma^{AA \rightarrow h}}{dy d^2 p_T}(y, p_T; W)}{N_{bin} \frac{d\sigma^{pp \rightarrow h}}{dy d^2 p_T}(y, p_T; W)}, \quad (1.3)$$

where  $y$  is the rapidity of the hadron,  $p_T$  is a transverse momentum,  $W$  is a nominal value of the center of mass energy in a nucleon collision, and  $N_{bin}$  is the average number of binary collisions of nucleons, most often calculated using the Glauber model [3]. Different effects arising from nuclear matter at extreme temperatures and pressures, such as shadowing, multiple parton scattering, and quenching or suppression of final state affect a dependence of nuclear modification factor  $R_{AA}$  on the transverse momentum in different ways. It is not easy to make an a priori prediction on the basis of these effects, because there is no exact model of a parton-nucleon interaction. However; the predicted schematic models are flexible enough to be able to describe the measured data [4].

## 1.4 Phase diagram of nuclear mater

Like in the classical phase transitions, a phase transition of nuclear matter can be observed when a sufficient energy is supplied to the system. At the present time, we are able to reach this energy (temperature and pressure) only in heavy ion collisions. Under these conditions the nuclear matter is able to change into a state called quark-gluon plasma, which is composed of asymptotically free quarks and gluons. The phase diagram of nuclear matter is shown in Figure 1.2, showing the dependence of the temperature on a baryon density.

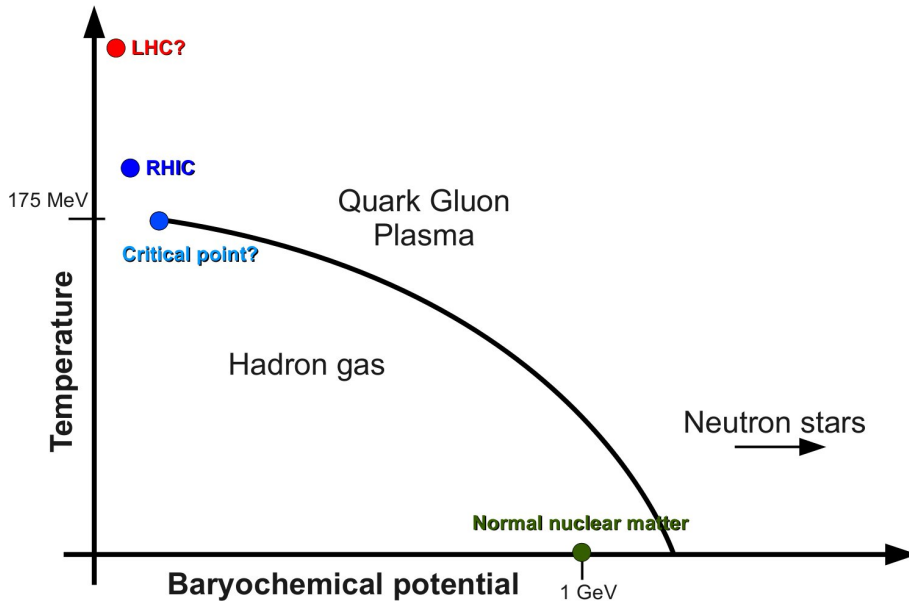


Figure 1.2: Phase transition diagram of nuclear matter as the temperature dependence of the baryon density

A hadronic gas at lower temperatures can be considered to be almost an ideal



gas. By increasing the temperature above the value of 100 MeV  $\pi$  mesons begin to form. The further increase of temperature promotes heavier resonances and baryon-antibaryon pairs. If the temperature rises over a certain value, the production of the particles becomes so strong that the power density of the hadronic gas exceeds the internal energy density of the individual components of the gas. You can imagine such a situation as hadrons (having the finite size) beginning to overlap. At this stage it is not possible to talk about the hadron gas, but usually the name *quark-gluon plasma* is used.

Quark-gluon plasma is formed at an early stage of a nucleus-nucleus collision. The cooling begins immediately by expansion and radiation, and it lasts until the moment when it reaches a critical temperature, and a phase transition into a state of hadronic gas occurs. Then the system breaks down into color neutral hadrons. In order accurately study the quark-gluon plasma, it is necessary to record the large number of particles that are emitted during the entire duration of the collision.

# Chapter 2

## The STAR experiment at accelerator RHIC

### 2.1 Relativistic Heavy Ion Collider, RHIC

Relativistic Heavy Ion Collider RHIC is located at Brookhaven National Laboratory (BNL) in the state New York. Since November 7, 2000 heavy ions are accelerated with an intention to study quark-gluon plasma, indications of which were observed at accelerator SPS [5]. In November 28, 2001 measurements of polarized proton proton collisions have started. A goal of these measurements is a detailed study of spin properties of a proton.

The advantage of RHIC accelerator design is an ability to accelerate the unequal types of particles. An example is the acceleration of ions of gold against protons or deuterons. The acceleration of particles is possible for a mass number  $A$  in interval between 1 and 200 and an atomic number  $Z$  in interval 1 to 80, where the ratio  $A / Z$  ranges 1 to 2.5. In order to accelerate the unequal particles in the accelerator, it is necessary to have two different circuits with large magnetic fields in the opposite direction. These circuits are able to operate with different magnetic fields, to achieve the same ratio of frequencies of bundles.

An arrangement of magnets in accelerator allows crossing of bundles at six points. One of the biggest advantages of the accelerator is the ability to accelerate gold ions in the energy range from injection energy up to the maximum energy. A typical accelerator operates only at the highest energies.

In Figure 2.1 layout of RHIC accelerator is displayed. The injection system prior to RHIC accelerator is composed of the Tandem Van de Graaff accelerator, Booster Synchrotron, Alternating Gradient Synchrotron (AGS).

Some of the parameters of RHIC accelerator are listed in Table 2.1.

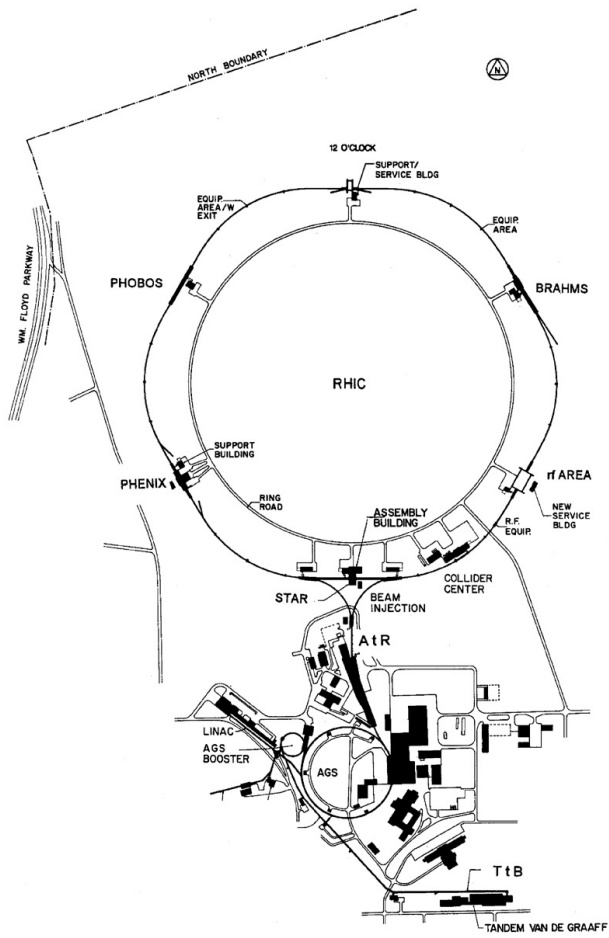


Figure 2.1: Schematic arrangement of RHIC accelerator and preaccelerate system [6]

Major parameters for the collider

Kinetic energy, injection top (each beam)	
Au	8.86–100 GeV/u
Protons	23,4–250 GeV
Luminosity, Au–Au @ 100 GeV/u & 10 h av.	$2 \cdot 10^{26} \text{cm}^{-2} \text{s}^{-1}$
No. of bunches/ring	56
No. of Au-ions/bunch	$1 \cdot 10^9$
Operational lifetime Au @ $\gamma > 30$ Diamond length	10 h
Circumference, $4\frac{3}{4}C_{AGS}$	3833.845 cm
Beam separation in arcs	90 cm
Number of crossing points	6
Free space at crossing point	$\pm 9$ m
Crossing angle, nominal (maximum)	0(<1.7) mrad
No. of dipoles (192/ring+12 common)	396
No. of quadrupoles (276 arc+216 insertion)	492
Operating temperature, helium refrigerant	< 4.6 K
Cool-down time, entire system	$\sim 7$ d
Filling time (each ring)	< 1 min
Beam stored energy	$\sim 200$ kJ

Table 2.1: Resume of some parameters of RHIC accelerator [6]

Run	species	$\sqrt{s}$ [GeV]
1	Au + Au	27.9
	Au + Au	65.2
2	Au + Au	100
	Au + Au	9.8
	p + p	100.2
3	d + Au	100.7—100.0
	p + p	100.2
4	Au + Au	100
	Au + Au	31.2
	p + p	100.2
5	Cu + Cu	100
	Cu + Cu	31.2
	Cu + Cu	11.2
	p + p	100.2
	p + p	204.9
6	p + p	100.2
	p + p	31.2
7	Au + Au	100
	Au + Au	4.6
8	Au + Au	100.7—100.0
	Au + Au	100.2
	Au + Au	4.6
9	p + p	249.9
	p + p	100.2
	p + p	100.2
10	Au + Au	100
	Au + Au	31.2
	Au + Au	19.5
	Au + Au	3.85
	Au + Au	5.75
11	p + p	249.9
	Au + Au	9.8
	Au + Au	100
	Au + Au	13.5
12	p + p	100.2
	p + p	254.9
	U + U	96.4
	Cu + Cu	99.9—100.0
13	p + p	254.9
14	Au + Au	7.3
	Au + Au	100
	h + Au	103.9—100.0
15	p + p <sup>19</sup>	100.2
	p + p	100
	p + Au	100

Table 2.2: List of all runs on RHIC accelerator, whit colliding species and energy of collision, run 15 is now in preparation  $\sqrt{s}$  [7]

## 2.2 STAR detector

STAR experiment displayed in Figure 2.2 is designed to investigate the properties of a strongly interacting matter. The main point of interest are signs of a quark-gluon plasma. The ability to measure many observables at the same time allows the study of the phase transition of a quark-gluon plasma to a hadron gas in ultrarelativistic ion collisions. Large acceptance of detector enables the accurate study of the characteristics event by event observables. The most important parts of the experiment are the time projection chamber TPC, the time of flight (TOF) detector and a barrel electromagnetic calorimeter BEMC. The entire system is surrounded by a magnet, which is at room temperature capable of producing a uniform magnetic field with a maximum intensity of 0.5 T. A produced magnetic field curves the paths of charged particles and we are able to roughly read off their momentum from the curvature of the helix in the known magnetic field [8].

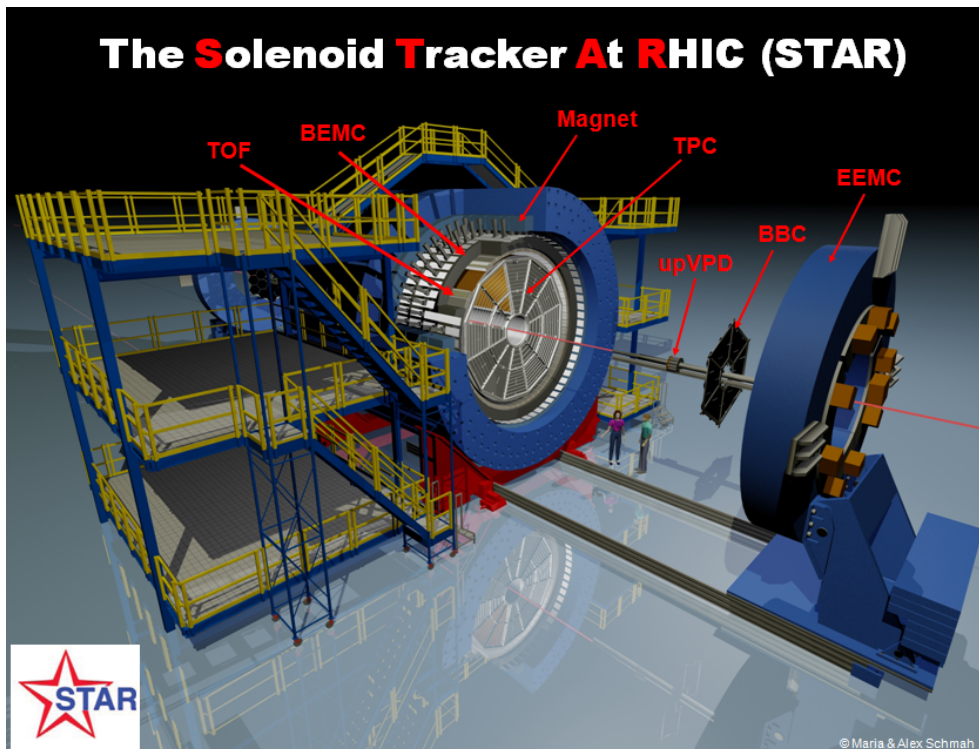


Figure 2.2: Scheme of STAR experiment with description of inner parts

## 2.2.1 Overview of subsystems of the STAR experiment

### Time Projection Chamber, TPC

Time Projection Chamber is used to detect tracks of charged particles at intervals of pseudorapidity  $|\eta| \leq 1.8$  with full azimuthal coverage and with a momentum greater than 100 MeV/c. The detector is able to identify particles by measuring the energy loss using the Bhete-Bloch formula

$$-\left\langle \frac{dE}{dx} \right\rangle = K z^2 \frac{Z}{A} \frac{1}{\beta^2} \left[ \frac{1}{2} \ln \frac{2m_e c^2 \beta^2 \gamma^2 T_{max}}{I^2} - \beta^2 - \frac{\delta(\beta\gamma)}{2} \right], \quad (2.1)$$

where  $z$  is the charge of the incident particle,  $Z$  is the atomic number of the absorber,  $A$  is the nucleon number of the absorber,  $\beta = \frac{v}{c}$  is the ratio of the speed of the incident particle and the speed of light,  $m_e$  is the mass of electron,  $\gamma$  is the Lorentz factor,  $T_{max}$  is the maximum transferred kinetic energy,  $I$  is the mean excitation energy and  $\delta(\beta\gamma)$  is the correction for the effects caused by density. The constant  $K$  is equal to

$$K = 4\pi N_A r_e^2 m_e c^2, \quad (2.2)$$

where  $N_A$  is Avogadro constant and  $r_e = \frac{e^2}{4\pi\epsilon_0 m_e c^2}$  is a classical radius of the electron [9].

The entire chamber of the detector is placed in a field of a solenoid magnet. The detector is 4.2 meters long and 4 meters in diameter, and the entire volume of the detector is hollow and filled with gas. The flying charged particles ionize the gas inside the volume of the detector. Created secondary electrons drift in the electric field towards a grounded readout surface at the end of the chamber. Formed ions are drained into the central membrane located in the middle of the detector, as seen in Figure 2.3. The membrane operates at the voltage of 28 kV.

The readout system is based on a multiwire readout chamber with readout pads. A total number of readout pads in the detector is 136 608. Drifting electrons in a strong field of anode create an avalanche of electron-ion pairs. Created positively charged ions shadow a negatively charged anode. In front of the anode is therefore placed a grid that is used to capture the positively charged ions. The avalanche created at the end of the electron path amplifies the signal from 1 000 to 3 000 times. The charge induced from avalanches is distributed among several neighboring readout pads. The position of the original path of a charged particle is therefore determined in small fractions of the width of the readout pads.

Detector chamber is filled with a gas P10 (10% methane, 90% argon) with a pressure adjusted to be 2 mbar higher than an atmospheric pressure. The electric field is adjusted so that the drifting speed of electrons is as stable as possible and consequently less sensitive to small variations in temperature and pressure of the gas.

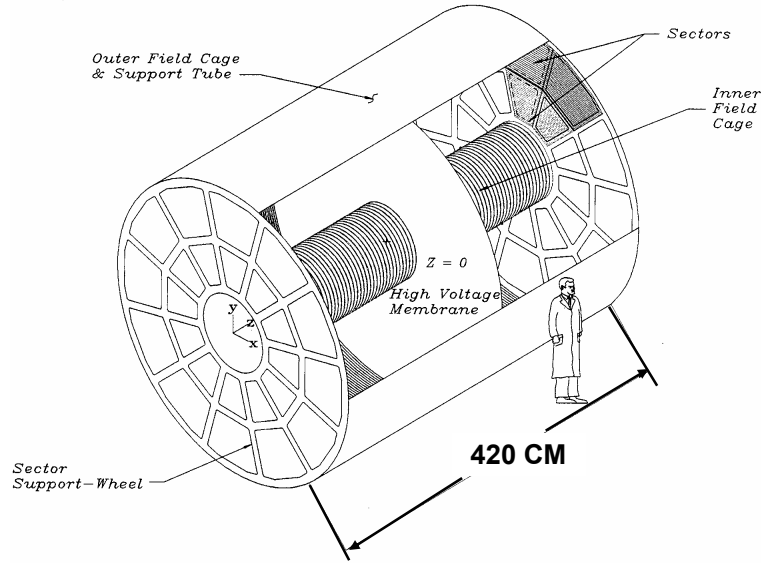


Figure 2.3: Scheme of Time Projection Chamber (TPC) with central membrane [8]

### Time of Flight detector, TOF

Time of Flight detector is used to improve the distinction of pions from the kaons in momentum range (0-2.5) GeV/c and to distinguish protons from the kaons in the interval (0-4.5) GeV/c. It has a time resolution better than 100 ps, and it covers the full azimuthal angle and pseudorapidity interval  $|\eta| \leq 1$ .

The detector works on the principle of measuring a time of particles with known trajectory. Starting time is measured by Position Vertex Detector (PVD) and the end time by Time of Flight detector (TOF). When data from TPC are added (path length and momentum), the particle can be identified. Time of Flight detector consists of 120 sections, each covering 6 degrees in the azimuthal direction and one unit of pseudorapidity ( $-1 < \eta < 0$  or  $0 < \eta < 1$ ) [10].

### Barrel Electromagnetic Calorimeter, BEMC

Barrel Electromagnetic Calorimeter is a sampling calorimeter composed of lead layers and a scintillation material. It covers a range of pseudorapidity  $|\eta| \leq 1$  and full azimuthal angle. It is designed to measure the energy of electrons, photons and hadrons decaying into lepton channels. The calorimeter is placed at a distance of 220 cm from the beam pipe.

The calorimeter consists of 120 modules with dimensions  $\Delta\eta \times \Delta\phi \simeq 1 \times 0.1$ . One calorimeter module consists of 21 scintillation plates, between which there is placed a 5 mm thick lead plate. Each scintillation plate is divided into 40 light-insulated tiles,



so there are 20 in the direction of pseudorapidity and 2 in the azimuthal direction. A light from 21 tiles from all layers is collected by single Photomultiplier Tube (PMT). One such part is called a cylindrical tower of electromagnetic calorimeter. In the calorimeter there are 4800 of such towers. The two innermost layers of the scintillator is more separately connected to a special photo detector, which is used to increase the resolution of photons and electrons from hadrons. Due to the splitting of the signal in the first two scintillating tiles, their thickness was designed to be 6 mm instead of the usual 5 mm of the other 19 [11].

## **The trigger system and data collection on the STAR experiment**

A data collection system has to be fast and flexible due to the fact that the data are coming from multiple detectors. Each event has a data size of the order of 200 megabytes and reaches a processing speed of 100 Hz [8].

In addition to the data collection it is important also to sort them. A classification is provided by so-called triggering system, which processes the data from the fastest detectors. From processed data the events that fill preset conditions are chosen. The trigger system is divided into three levels 0 , 1 and 2, where 0 is the fastest degree, and the other two are used in more sophisticated methods. STAR experiment has also the third level trigger, which is able to completely reconstruct the event in real time by using the so-called CPU farm. The trigger is capable of handling a central Au + Au collision with a frequency of 50 Hz, including a rapid analysis of some important observables (momentum of a particle, ionization energy loss). The output of this trigger can also be a visual demonstration of event at TPC 2.4. Fast detectors, which are used for data processing triggering system are ZDC and CTB .

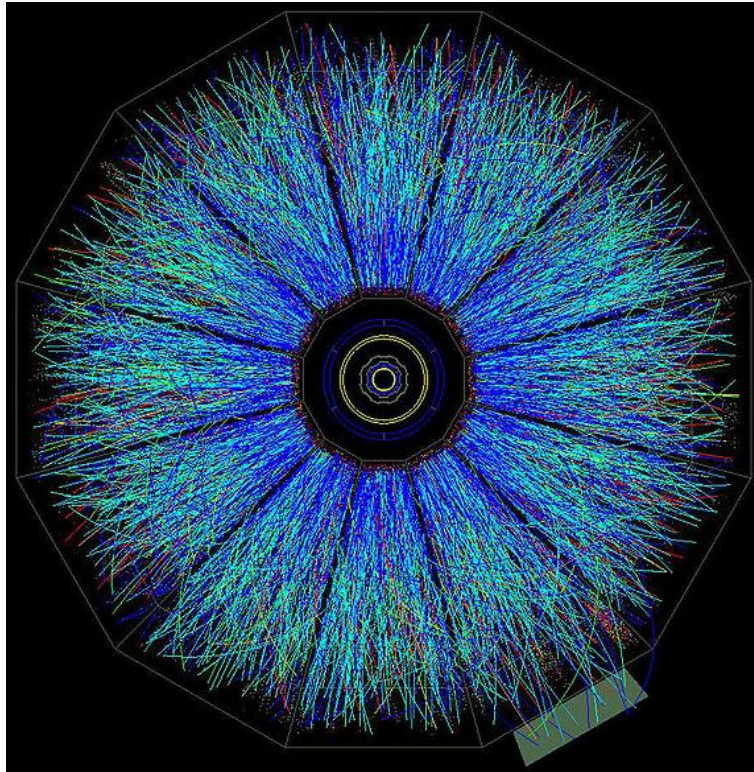


Figure 2.4: Particle tracks recorded TPC detector in collision of gold nuclei at RHIC at maximum energy of accelerator



# Chapter 3

## Production mechanism of $J/\psi$

### 3.1 Introduction

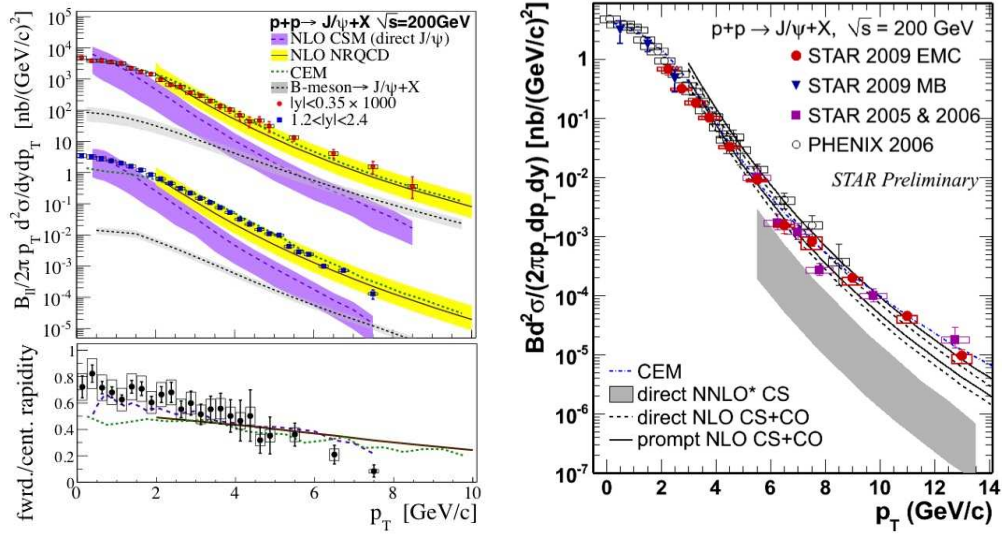
There are several models of  $J/\psi$  production mechanism which describe well measured cross sections [12]. However; cross section measurements are not enough to distinguish between the quarkonium production models as you can see in Figure ???. A measured data does include feed-down from b quark decays and decays of excited states of a charmonium.

On the one hand, the non-relativistic quantum chromodynamics calculations dominated by the Color Octet component (Figure 3.2b) predict that at asymptotically high transverse momentum  $p_T$  direct produced  $J/\psi$  and  $\psi'$  mesons are almost fully transversely polarized. This model is in a good agreement with with observed  $p_T$  spectra of  $J/\psi$  in experiments at different energies [15].

On the other hand, a new next-to-leading-order calculation of Color Singlet Model (Figure 3.2a) predicts longitudinal  $J/\psi$  polarization in the helicity frame at low and mid- $p_T$  at mid rapidity [16].

For low- $p_T$  region, measurements of the polarization of  $J/\psi$  at PHENIX experiment at  $\sqrt{s_{NN}}=200$  GeV are in a good agreement with the Color Octet Model prediction. However; at low- $p_T$  the data are not able to distinguish between Color Octet Model and Color Singlet Model, since in this  $p_T$  region the both models predictions are similar. Furthermore; Color Octet Model failed to describe  $J/\psi$  polarization measurements in CDF experiment at FermiLab at energy  $\sqrt{s_{NN}}=1.96$  TeV at high  $p_T$  ( $p_T>5$  GeV/c).

The measurement of the  $J/\psi$  polarization at high- $p_T$  region can distinguish between the Color Octet Model and Color Singlet Model. With increasing  $p_T$ , a polarization in the Color Octet Model leads to a transverse polarization, while the Color Singlet Model continues to predict a longitudinal polarization with no or small dependence on  $p_T$ .



(a) PHENIX  $J/\psi$   $p_T$  spectrum measurement at energy  $\sqrt{s_{NN}} = 200$  GeV including comparison with different model predictions [13]

(b) STAR  $J/\psi$   $p_T$  spectrum measurement at energy  $\sqrt{s_{NN}} = 200$  GeV including comparison with different model predictions [14]

Figure 3.1: Spectrum of transverse momentum  $p_T$  of  $J/\psi$  measured at PHENIX and STAR with comparison of production models

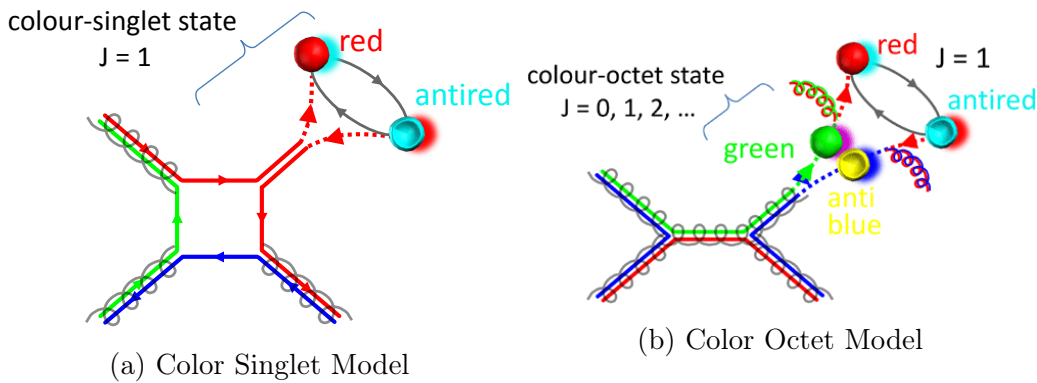


Figure 3.2: Graphic representation of production models

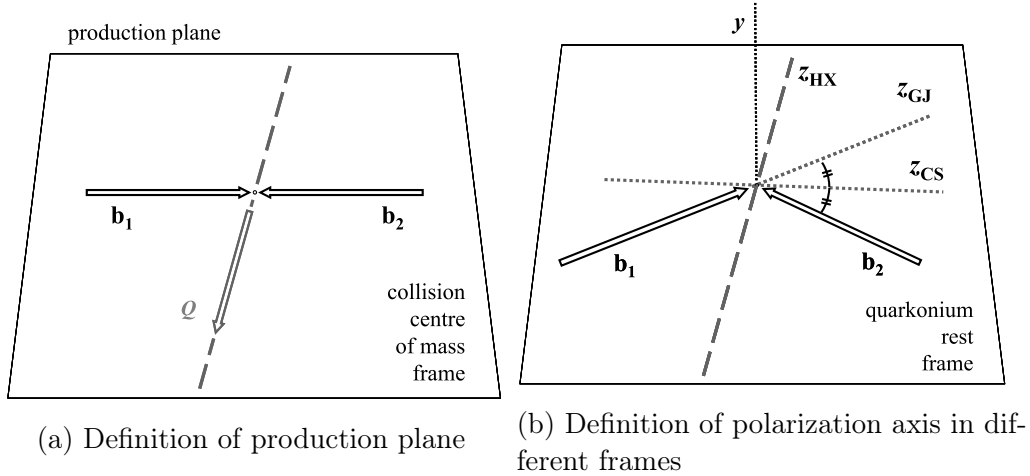


Figure 3.3: Definition and orientation of reference frame

### 3.1.1 Reference frame

For a definition of a polarization it is very important to choose the rest frame. First we defined the production plane by a vector in the direction of the beam and a vector of the produced  $J/\psi$  as is seen in Figure 3.3a, left hand side. The next step is to define a polarization axis  $z$ . There are three common ways to define a polarization axis and to determine specific frames to measure a polarization of  $J/\psi$  (Figure 3.3a, right hand side). The most common frame which is used in collider experiments is Helicity frame (HX), which defines  $z$  axis along  $J/\psi$  direction in the laboratory frame. Recently the Collins-Soper frame (CS) was also used. It is defined as a bisector of the angle formed by one beam direction and the direction of the opposite beam. In fixed target experiments the Gottfried-Jackson frame (GJ) is mostly used.

Finally, we can define decay angular coefficients. Angular distribution can be written as

$$\frac{d\sigma}{d\cos\theta d\varphi} \propto 1 + \lambda_\theta \cos^2(\theta) + \lambda_\varphi \sin^2(\theta) \cos(2\varphi) + \lambda_{\theta\varphi} \sin(2\theta) \cos(\varphi) \quad (3.1)$$

where  $\theta$  is a polar angle, defined as an angle between positron momentum in the  $J/\psi$  rest frame and the polarization axis  $z$ .  $\phi$  is an azimuthal angle. Definition of the angles is shown in Figure 3.4.  $\lambda_\theta$  coefficient is usually called a polarization parameter. In general,  $\lambda_\theta = -1$  means a full longitudinal polarization and  $\lambda_\theta = +1$  a full transverse polarization, if we have assumed that there is no dependence on the azimuthal angle.

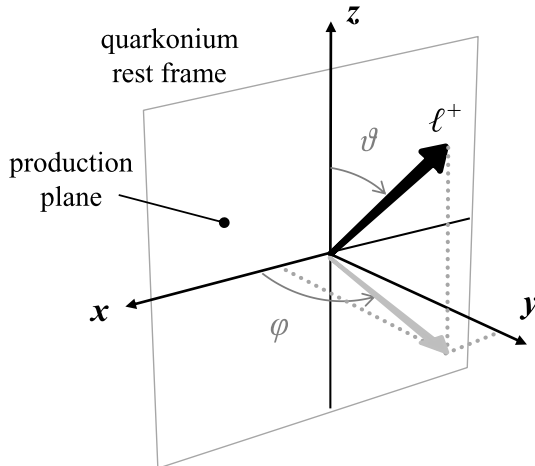


Figure 3.4: Definition of polarization angles

## 3.2 Tevatron and LHC measurement of polarization

In Figure 3.5, NLO NRQCD predictions for  $\lambda_\theta$  and  $\lambda_\varphi$  as functions of  $p_T$  in the helicity and Collins-Soper frames with the measurements by CDF and ALICE are shown. Since the parameters  $\lambda_\theta$  and  $\lambda_\varphi$  are very insensitive to the precise value of  $\sqrt{s_{NN}}$ , it is safe to overlap the data for  $\sqrt{s_{NN}} = 1.8$  TeV with the predictions for  $\sqrt{s_{NN}} = 1.96$  TeV.

Comparison of leading order NRQCD prediction for  $\lambda_\theta$  in Figure 3.5(a) with direct  $J/\psi$  production in Figure 3.5(b), it can be seen that for  $p_T \gg 2m_c$ , results are almost the same, the transition from the Tevatron to LHC and from central ( $|y| < 0.6$ ) to the forward ( $2.5 < y < 4$ ) rapidity region, this all valid only if the helicity image. However, the transition from the helicity frame to Collins-Soper frame strongly affect the various  $p_T$  distribution as comparing Figure 3.5(b) and 3.5(c) is shown. The most significant effect occurs for  $\lambda_\theta$ , which results NLO CSM and NRQCD is approximately inverted. The theoretical uncertainty due to scale differences gradually decline with increasing of value of  $p_T$ . This behavior only reflects the asymptotic freedom.

## 3.3 STAR measurement of polarization

The  $p_T$ -dependent  $J/\psi$  polarization parameter  $\lambda_\theta$  is shown in Figure 3.6. The data from measurements in PHENIX are also included in this Figure. The sample includes directly produced  $J/\psi$  as well as the  $J/\psi$  from the feed-down from the higher excited states,  $\chi_C$  and  $\psi'$  ( $33 \pm 5\%$ ) and from the B meson feed-down ( $10-25\%$  or  $4 < p_T < 12$  GeV/c). The result is also compared with two model predictions

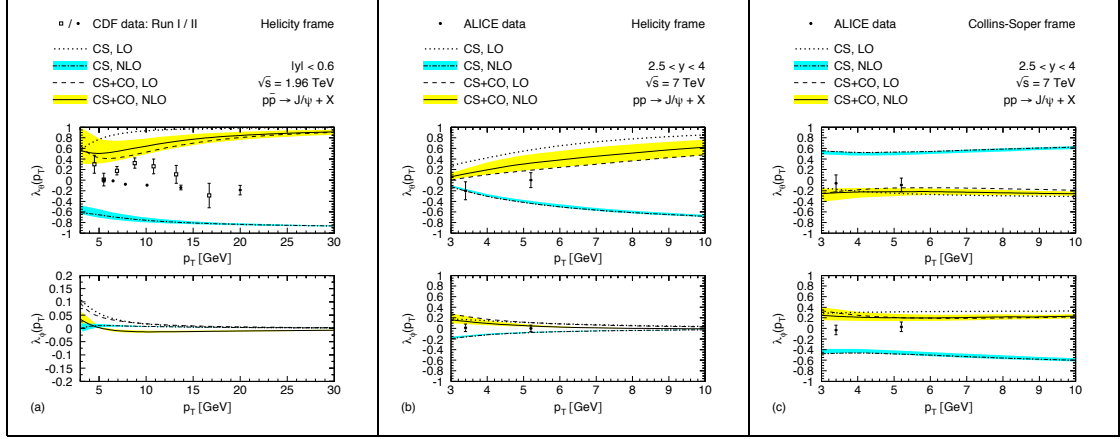


Figure 3.5: NLO NRQCD predictions for  $\lambda_\theta$  and  $\lambda_\phi$  as functions of  $p_T$  in the helicity and Collins-Soper frames including theoretical uncertainties (shaded/yellow bands) compared to CDF and ALICE data. For comparison, also the NLO CSM (dot-dashed lines) predictions including theoretical uncertainties (hatched/blue bands) as well as the LO NRQCD (dashed lines) and LO CSM (dotted lines) ones are shown. [17]

for the  $\lambda_\theta$  at mid-rapidity: The prediction of COM for direct  $J/\psi$  production (gray shaded area) goes towards the transverse  $J/\psi$  polarization as  $p_T$  increases. This trend is different from what is seen in the RHIC data. Green dashed lines represent a range of  $\lambda_\theta$  for the direct  $J/\psi$  production from the NLO+CSM prediction and an extrapolation of  $\lambda_\theta$  for the prompt  $J/\psi$  production is shown as the hatched blue band. This model predicts a weak  $\lambda_\theta$   $p_T$ -dependence, and within the experimental and theoretical uncertainties the RHIC result is consistent with the NLO+ CSM model prediction. A blue line in Figure 3.6 is a linear fit of the data from PHENIX measurements and the data from the STAR measurement with  $p_T > 3$  GeV/c. This fit suggests that for higher  $p_T$  the fitted curve tends towards the longitudinal polarization.



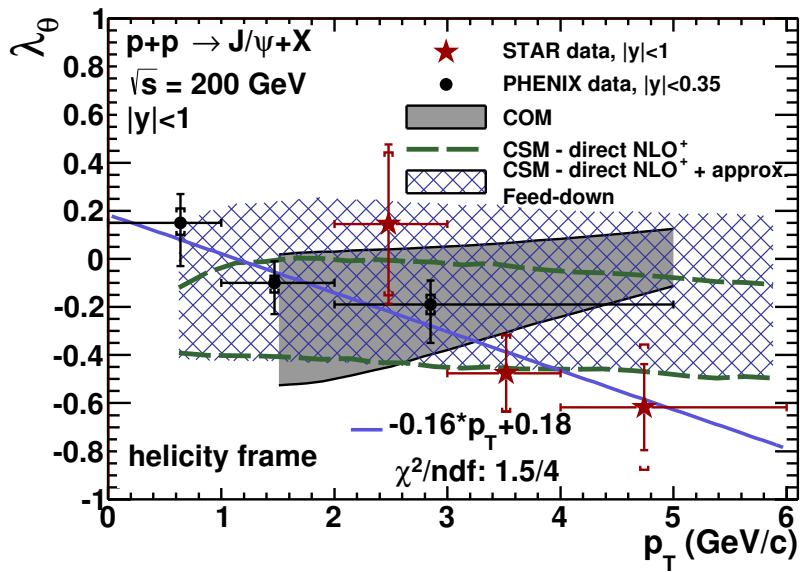


Figure 3.6: The polarization parameter  $\lambda_\theta$  as a function of  $J/\psi$   $p_T$  (red stars) for  $|y| < 1$  in p+p collisions at  $\sqrt{s_{NN}} = 200$  GeV together with the PHENIX result is shown as black circles. The results are compared with two model predictions: NLO+Color Singlet Model (CSM) (green dashed lines) and NRQCD calculations with Color Octet Model contributions (COM) (gray shaded area).

# Chapter 4

## Analysis of simulated data

### 4.1 Methods of analysis of polarization

An analysis of polarization is in this work done in the helicity frame. It is focused on a polar angle  $\theta$  and also on an azimuthal angle  $\varphi$ . We are interested in parameters  $\lambda_\theta$  and  $\lambda_\varphi$  defined in equation (3.1). To extract the individual parameters we have to integrate the distribution over each of the angles separately. We obtain the angular distribution integrated over  $\varphi$ :

$$W(\cos \theta) \propto 1 + \lambda_\theta \cos^2 \theta, \quad (4.1)$$

and the distribution integrated over  $\theta$ :

$$W(\varphi) \propto 1 + \frac{2\lambda_\varphi}{3 + \lambda_\theta} \cos(2\varphi). \quad (4.2)$$

When we extract the polarization parameters  $\lambda_\theta$  a  $\lambda_\varphi$ , we can use a frame-invariant approach. By combination of the polarization parameters we can obtain a frame invariant quantity  $\tilde{\lambda}$  which is defined as

$$\tilde{\lambda} = \frac{\lambda_\theta + 3\lambda_\varphi}{1 - \lambda_\varphi}. \quad (4.3)$$

This variable is better for comparing the polarization in different experiments since this invariant parameter is less acceptance-dependent than the parameters  $\lambda_\varphi$ ,  $\lambda_\theta$  and  $\lambda_{\theta\varphi}$  [18].

### 4.2 Embedding

In this analysis  $J/\psi$  is reconstructed from dielectron decay channel  $J/\psi \rightarrow e^+e^-$  with branching ratio  $\text{BR} = 5.94 \pm 0.06 \%$  [19]. We are interested in high- $p_T$   $J/\psi$

which have at least one of the decaying electrons with high-enough  $p_T$  to trigger High Tower trigger.

An embedding is a process when Monte Carlo simulated  $J/\psi$  data are embedded in the real data. We used the data from proton-proton collisions at energy  $\sqrt{s_{NN}} = 500$  GeV. To save the computing time the embedded  $J/\psi$  are implemented with a flat  $p_T$  distribution in range  $0 < p_T < 30$  GeV/c and a flat rapidity distribution in range  $-1.5 < y < 1.5$ . To correct this non-physical behavior the weight according to the real shapes of  $p_T$  spectra is used, and it is defined as

$$w = p_T \cdot 2.939 \cdot \left( e^{-0.912 \cdot p_T + 0.03815 \cdot p_T^2} + \frac{p_T}{2.904} \right)^{-6.812}. \quad (4.4)$$

The rapidity distribution remains flat, because the rapidity dependence does not have a strong influence in our analysis. At each event they were randomly generated five  $J/\psi$ 's, which decay only into the dileptonic channel. One million of such events was generated. The process of embedding is described in a flowchart in Figure 4.1.

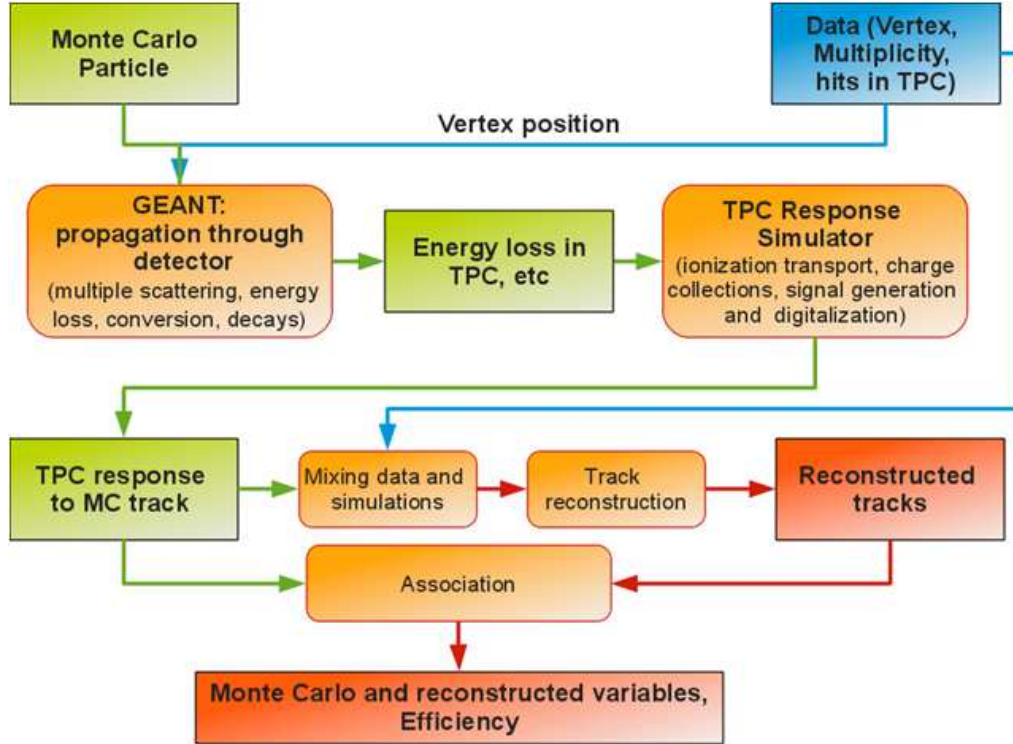


Figure 4.1: Flowchart illustrating embedding process

### 4.3 $\varphi$ measurement

In Figure 4.2 the distribution of  $\varphi$  angle is shown. There are no cuts applied, and as we expected the distribution is flat.

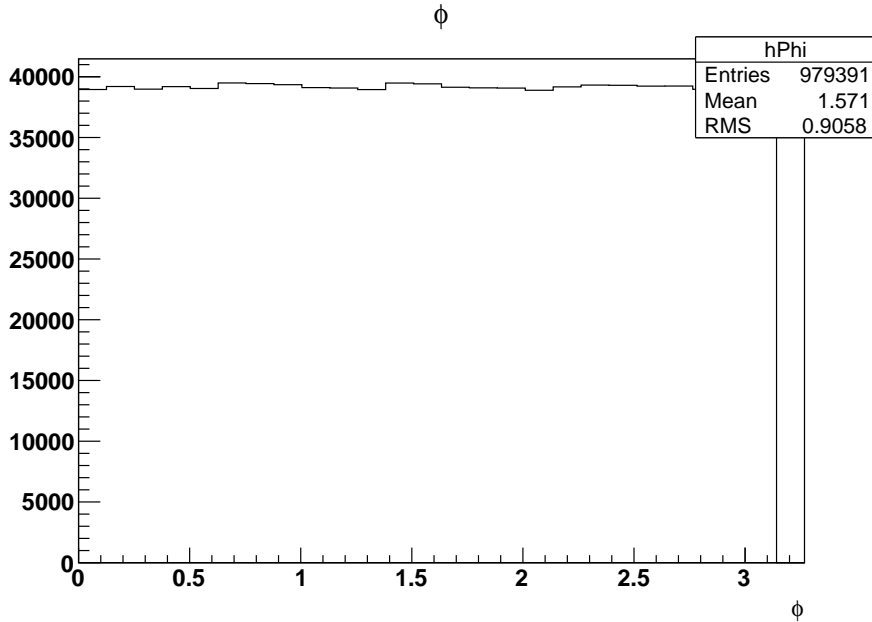


Figure 4.2: Distribution of angle  $\varphi$  in simulate data with no additional cuts

Non-flat distribution in Figure 4.3 is caused by weighting the signal with the function (4.4). There are several cuts applied. Track quality cuts and acceptance cuts are applied in this figure as well. List of this cuts including their explanation is in Table 4.1.

The distribution in Figure 4.4 in contrary to the previous figure has also High Tower trigger applied. This means that at least one of the electrons fired this trigger. In this manner we are keeping only the candidates for  $J/\psi$  with high enough  $p_T$  important for our analysis.

Cut	Name	Comment
$nFitPts \geq 15$	minimum number of points in track fit	good quality of track and resolution of track momentum
$nFitPts/nFitPtsMax \geq 0.52$	ratio of number of points in track fit and maximum number of available points in fitting procedure	avoiding split tracks
$DCA \leq 2$ cm	closest approach to the primary vertex	$J/\psi$ have short lifetime so it decays very close to the primary vertex
$ \eta  \geq 1$	pseudorapidity cut	
$p_T \geq 0.5$ GeV/c	transverse momentum cut for a single track	low number allows the acceptance of electrons in longitudinal direction
$-1 < n\sigma_e < 2$	cut selecting electrons in TPC	asymmetry of this cut rejects lots of hadrons, especially pions with momentum $p \gtrsim 1.4$ GeV/c
$ 1/\beta - 1  \leq 0.003$	cut selecting electrons in TOF	since hadrons are slower than electrons, this cut rejects hadrons especially with lower momentum ( $p < 1.4$ GeV/c)
$ y_{local}  < 2$ cm	TOF matching	this cut ensures that the tracks from TPC match the hits in TOF detector
$E/p \geq 0.5c$	BEMC cut rejecting hadrons	Electrons, in contrary to hadrons, should deposit all of its energy in calorimeter

Table 4.1: List of cuts applied to identify electrons and guarantee track quality

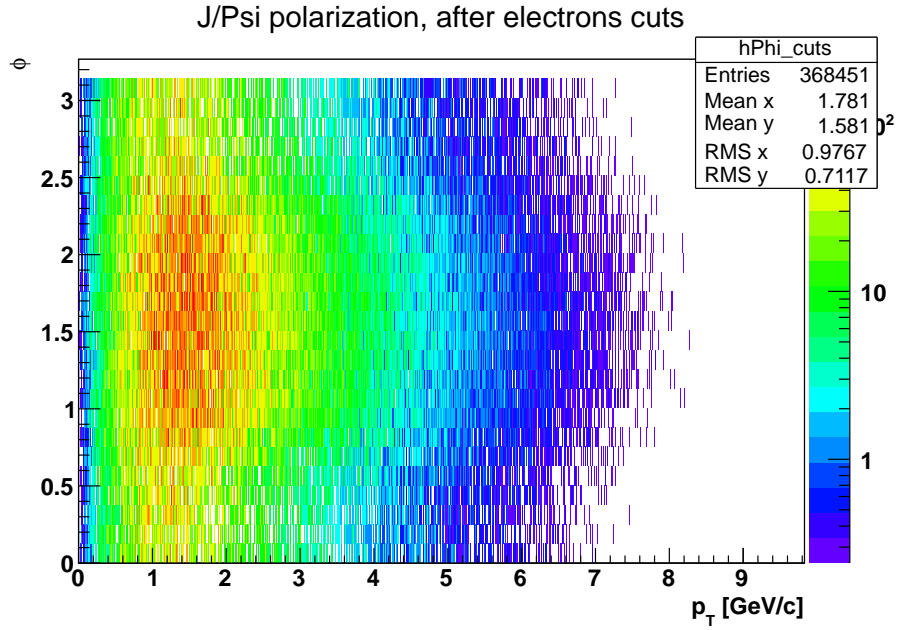


Figure 4.3: Distribution of angle  $\varphi$  in simulated data weighted with (4.4) and adapted for acceptance for electrons

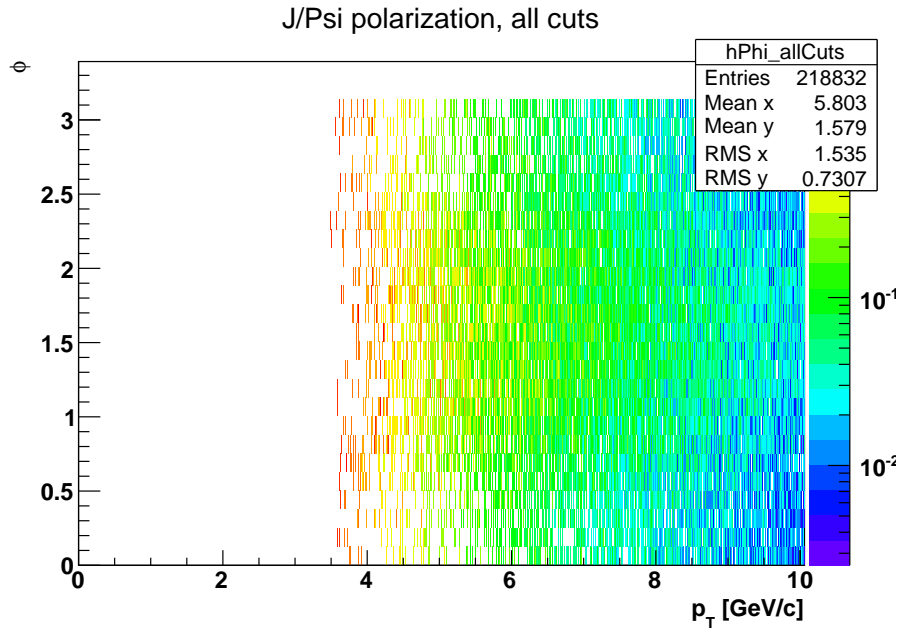


Figure 4.4: Distribution of angle  $\varphi$  for various  $p_T$  in simulated data weighted with (4.4) and adapted for acceptance for electrons, with all cuts and a trigger



# Conclusion

In this work we have analyzed embedded data in proton-proton collisions at energy  $\sqrt{s_{NN}} = 500$  GeV. We have focused mainly on extracting the azimuthal distribution of the polarization of meson  $J/\psi$ . We were able to apply cuts for track quality, acceptance and High Tower trigger. The weight to change a flat distribution to the physical shape was applied too.

The next step will be to check the efficiency of the analysis by comparing the data we have extracted using the analysis with the data there were put in with embedding.

The point of this study is to ensure that our analysis is efficient enough, and we do not reject a significant amount of  $J/\psi$ 's.

These measurements in general are important in order to understand the production mechanism of quarkonia. It is important to determine which of given theoretical models better describe the production of  $J/\psi$ . Some assumptions on the polarization of  $J/\psi$  are based on a fact that the distribution in azimuthal angle  $\varphi$  is flat.





# Bibliography

- [1] L Zielinski. Physics folklore. <http://ed.fnal.gov/samplers/hspphys/folklore.html>, 2006.
- [2] R. Vogt. *Ultrarelativistic Heavy-Ion Collisions*. Elsevier Science, 2007.
- [3] M. L. Miller, K. Reygers, S. J. Sanders, and P. Steinberg. Glauber modeling in high energy nuclear collisions. *Ann.Rev.Nucl.Part.Sci.*, 57:205–243, 2007.
- [4] A. Szczurek and A. Budzanowski. Fermi motion and nuclear modification factor. *Mod.Phys.Lett.*, A19:1669–1680, 2004.
- [5] M. Gazdzicki. Quark gluon plasma in a + a collisions at cern sps. (hep-ph/9806257), 1998.
- [6] H. et. al Hahn. The rhic design overview. *Nuclear Instruments and Methods in Physics Research Section A: Accelerators, Spectrometers, Detectors and Associated Equipment*, 499(2-3):245–263, March 2003.
- [7] Fischer W. Run overview of the relativistic heavy ion collider. <http://www.rhichome.bnl.gov/RHIC/Runs/>, June 2013.
- [8] K.H. Ackermann et al. Star detector overview. *Nuclear Instruments and Methods in Physics Research Section A: Accelerators, Spectrometers, Detectors and Associated Equipment*, 499(2):624–632, 2003.
- [9] J. Beringer et al. Review of Particle Physics (RPP). *Phys.Rev.*, D86:010001, 2012.
- [10] Kajimoto K. *A large area time of flight detector for the STAR experiment at RHIC*. PhD thesis, The University of Texas at Austin, 2010.
- [11] T.M. Cormier, A.I. Pavlinov, M.V. Rykov, V.L. Rykov, and K.E. Shesternanov. STAR barrel electromagnetic calorimeter absolute calibration using 'minimum ionizing particles' from collisions at RHIC. *Nucl.Instrum.Meth.*, A483:734–746, 2002.

- [12] J. Adams et al. Identified hadron spectra at large transverse momentum in p+p and d+Au collisions at  $\sqrt{s} = 200$ -GeV. *Phys.Lett.*, B637:161–169, 2006.
- [13] A. et al. Adare. Ground and excited state charmonium production in  $p + p$  collisions at  $\sqrt{s} = 200$  GeV. *Phys. Rev. D*, 85:092004, May 2012.
- [14] Barbara Trzeciak. Quarkonia production in the STAR experiment. *Nucl.Phys.*, A904-905:607c–610c, 2013.
- [15] Eric Braaten, Sean Fleming, and Tzu Chiang Yuan. Production of heavy quarkonium in high-energy colliders. *Ann.Rev.Nucl.Part.Sci.*, 46:197–235, 1996.
- [16] Eric Braaten, Bernd A. Kniehl, and Jungil Lee. Polarization of prompt  $J/\psi$  at the Tevatron. *Phys.Rev.*, D62:094005, 2000.
- [17] Mathias Butenschoen and Bernd A. Kniehl.  $J/\psi$  polarization at Tevatron and LHC: Nonrelativistic-QCD factorization at the crossroads. *Phys.Rev.Lett.*, 108:172002, 2012.
- [18] Pietro Faccioli, Carlos Lourenco, Joao Seixas, and Hermine K. Wohri. Towards the experimental clarification of quarkonium polarization. *Eur.Phys.J.*, C69:657–673, 2010.
- [19] J. Beringer et al. Review of Particle Physics (RPP). *Phys.Rev.*, D86:010001, 2012.